

Flow Characterisation of Porous Ultra-High-Temperature-Ceramics for Transpiration Cooling

Hassan Saad Ifti^{*}, Tobias Hermann[†], and Matthew McGilvray[‡]
University of Oxford, Oxford, OX2 0ES, United Kingdom

Laura Larrimbe[§], Rowan Hedgecock[¶], and Luc Vandeperre^{||}
Imperial College London, London, SW7 2AZ, United Kingdom

Porous Ultra-High-Temperature-Ceramics (UHTC) are a candidate group of materials for transpiration cooling of hypersonic vehicles due to their exceptionally high melting point, typically above 3000 K. Their high operating temperature permits a higher amount of radiative cooling than that achievable with conventional materials, which reduces the required coolant mass flow rate to cool the surface. This work experimentally examines the internal and external flow behaviour of porous UHTC made of zirconium diboride (ZrB_2) for the purpose of transpiration cooling. A dedicated ISO standard permeability test rig was built. The outflow velocity distribution was acquired employing miniature hot-wire anemometry. The data obtained for the pressure loss across the porous samples agree with the Darcy-Forchheimer model for flow in porous media; respective Darcy and Forchheimer permeability coefficients are calculated and reported. Cleaning the surface of the samples using sandpaper or an ultrasonic bath raised the permeability coefficient by up to 19%. The outflow velocity maps exhibit a good flow uniformity with an average standard deviation of 25.1% with respect to the mean value. Individual jets are absent, and the velocity varies within the same order of magnitude.

I. Introduction

A hypersonic vehicle experiences extreme heat fluxes due to aerodynamic heating [1], which becomes detrimental for the vehicle at very high Mach numbers, especially during the re-entry into Earth's atmosphere or a planetary entry, e.g. into Mars. At re-entry speeds (approximately Mach 25), it becomes extremely challenging for an entry body to safely return back to Earth due to the high heat flux on the vehicle's surface [2]. Several types of Thermal Protection

^{*}DPhil Candidate, Oxford Thermofluids Institute, Department of Engineering Science, University of Oxford, Southwell Building, Osney Mead.
Email: saad.ifti@eng.ox.ac.uk

[†]Lecturer, Oxford Thermofluids Institute, Department of Engineering Science, University of Oxford, Southwell Building, Osney Mead.

[‡]Associate Professor, Oxford Thermofluids Institute, Department of Engineering Science, University of Oxford, Southwell Building, Osney Mead.

[§]Former Postdoctoral Associate, Department of Materials, Imperial College London, Royal School of Mines, Exhibition Road.

[¶]PhD Student, Department of Materials, Imperial College London, Royal School of Mines, Exhibition Road.

^{||}Professor, Department of Materials, Imperial College London, Royal School of Mines, Exhibition Road.

This work builds on, and is a continuation of, the conference paper AIAA 2018-5167 published in 22nd AIAA International Space Planes and Hypersonics Systems and Technologies Conference, 17-19 September 2018, Orlando, FL, USA.

Systems (TPS) are therefore in use today that protect the payload from overheating.

In addition to the TPS needs of hypersonic spacecraft in operation today – such as the carbon-phenolic ablative heat shields on returning capsules – envisaged re-usable hypersonic passenger vehicles, e.g. the Skylon [3], will require protection from high heat loads [4]. The recent unveiling of Boeing’s hypersonic passenger jet and Lockheed Martin’s SR-72 highlights the interest in sustained, atmospheric hypersonic flight, where high heat fluxes will occur on the leading edges. Although the state-of-the-art heat mitigation techniques – e.g. passive methods such as heat sinks and semi-passive methods such as ablation [5] – are successful for vehicles in operation at present, these conventional thermal protection systems have a low degree of re-usability. This limitation results in a higher cost of payload transfer. A re-usable, high-performing thermal protection system could therefore drive this cost down, making space and hypersonic flight more accessible. The pursuit of a novel, re-usable TPS is critical to both present and future hypersonic flight. Amongst the possible re-usable TPS candidates, transpiration cooling has shown promise [6, 7]. Although it comes with added complexity – and could add weight to the vehicle – transpiration cooling has the potential to minimise or remove the use of ablative material and increase re-usability of spacecraft or hypersonic cruise vehicles.

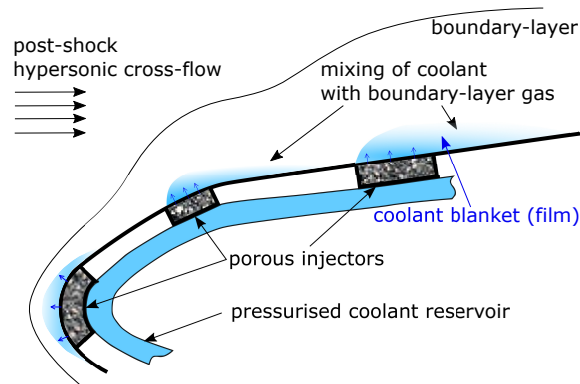


Fig. 1 A leading edge of a hypersonic vehicle with porous, transpiration cooling injectors (not to scale).

The cooling process by transpiration generally takes place by three different effects. A schematic of the process is shown in Fig. 1. The pressurised coolant gas in the reservoir seeps through the porous material and thereby absorbs the heat from it by convection. This keeps cooling the material as long as there is a temperature gradient between the material and the coolant gas, which accounts for the first effect. The second effect comes into play when the injected coolant gas leaves the porous material and convects downstream (see Fig. 1). This forms a thin blanket or film of coolant gas, which acts as an insulation between the wall and the incoming hot gas flow and thus prevents the wall from overheating. In addition, if the material can be raised to a higher temperature, the rate of heat radiated back into space can be increased. This however requires the avoidance of oxidation of the material in use, which can be the third effect of transpiration cooling if an inert gas is used as the coolant [8]. This effect can additionally decrease the rate of plasma recombination

and thereby further reduce heating.

The amount of coolant can be actively varied by modifying the injection rates, although this is limited due to the potential lift-off of the jets that could lead to early transition of the boundary-layer [9]. The boundary-layer thickens due to the blanket (film) of coolant gas as shown in Fig. 1. The coolant gas eventually starts mixing with the boundary-layer gas; consequently, the insulating blanket diminishes at some downstream location depending on the strength of mixing. This length of the effective insulating blanket (i.e. effectiveness), the mixing, and the injection are of importance. However, to fully comprehend these complex phenomena, it is sensible to first understand the behaviour of the outflow through porous media without the complications introduced by the hypersonic cross-flow. In a separate work [10], the authors showed that a non-uniform injector leads to a non-uniform film downstream. It is therefore important to analyse the outflow characteristics of a particular sample in order to interpret the respective influence of coolant injection into a cross-flow.

Various materials from metals to ceramic matrix composites (CMC) have been investigated as potential porous media for hypersonic application. Carbon-carbon (C/C) type CMC has been used extensively for transpiration cooling experiments by DLR [7, 11, 12], ITLR [13, 14], and IRS [15]. The reason for this choice lies in its high operational temperature of approximately 1800 K [13], producibility, low density, and, foremost, high specific strength and modulus [16]. Gascoin et al. [17–19] performed permeability tests on stainless steel, bronze, and CMCs and reported their permeability coefficients. Further, Dittert et al. [11] showed that the outflow of porous CMC exhibits significant local non-uniformities, which could potentially lead to film separation or early transition of the boundary-layer.

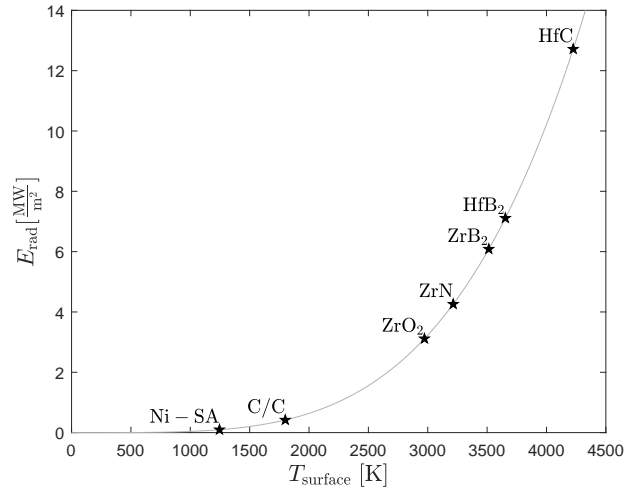


Fig. 2 Cooling capability by radiation versus melting point of Ni-SA, C/C, and a number of UHTCs assuming an emissivity of 0.7 (the grey, solid line denotes the Stefan-Boltzmann law).

UHTCs have an exceptionally high melting point, generally above 3000 K [20]. This property enables them to have higher surface temperatures that result in a higher amount of cooling by radiation (heat radiated back to space) compared

to conventional materials as shown in Fig. 2. Radiative cooling of UHTCs (ZrO_2 to HfC) is multiple times higher than that of carbon-carbon (C/C) type CMC or Nickel Super Alloys (Ni-SA). A higher amount of radiative cooling allows for a lower coolant mass injection rate required to cool the surface. This reduces the required coolant mass that needs to be carried in the vehicle and thereby increases its payload capacity. Although UHTCs (ZrN to HfC in Fig. 2) oxidise at higher temperature, transpiration cooling with an inert gas as the coolant can mitigate oxidation [8] and thereby enable an operating temperature that is close to their respective melting point. Thus, transpiration cooling employing UHTCs as the porous injector becomes a compelling technology for thermal management of a hypersonic vehicle, which makes UHTCs an exceptionally promising candidate group of materials for transpiration cooling. However, data on flow characteristics of transpiring porous UHTCs are not available in the literature.

In this paper, porous samples made of zirconium diboride (ZrB_2), a UHTC, are experimentally studied for their permeability and outflow characteristics. This is the first time a porous UHTC's flow characteristics are examined for the purpose of transpiration cooling. The Darcy and Forchheimer coefficients are determined for samples of different porous structures and porosities using a dedicated ISO standard test rig (BS EN ISO 4022:2006, [21]). The uniformity and jet behaviour of the outflow are measured and observed using miniature hot-wire anemometry. In contrast to conventional pitot probes, miniature hot-wire probes feature a smaller sensor (wire dimensions: $5\text{ }\mu\text{m}$ in diameter, 1.25 mm in length) that allows for a finer spatial resolution when traversing over an area.

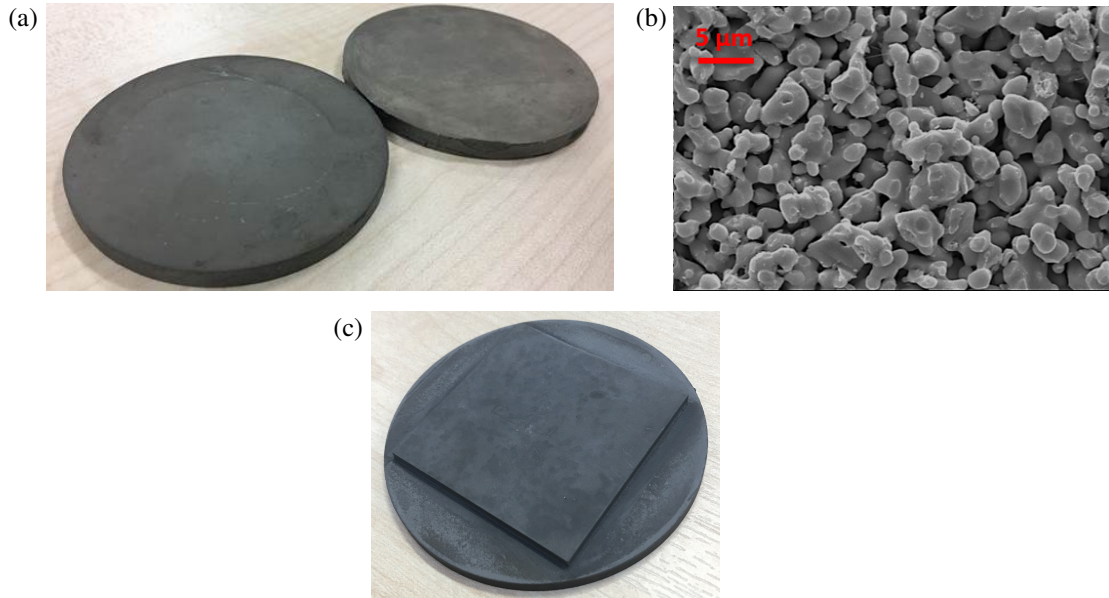
II. UHTC Samples

The porous UHTC samples used for this paper are made of zirconium diboride (ZrB_2), which has a density of $\rho_{\phi=100\%} = 6080\text{ kg/m}^3$ in a 100% densified state. The melting point and thermal conductivity of ZrB_2 are 3505 K [20] and 56 W/mK [22], respectively. The different porosities and porous structures in these samples are achieved by partial sintering (see Fig. 3). Partial sintering is the most conventional technique for making porous ceramics. The pores are produced by incomplete fusion of the particles. As it can be seen in Fig. 3b, pores with a refined size remain among the grains after the sintering in this method. Commercial ZrB_2 powder (grade B, H.C. Starck, Germany) was used as the starting material. The powder was loaded into a 70 mm , or 80 mm , diameter graphite die. To minimise reaction between the graphite die and precursor powder, the inner walls of the dies were lined with thin graphite paper before the powder was loaded. Hot pressing was completed in a graphite resistance-heated vacuum hot press furnace. During exploration, the final hot pressing temperatures were varied between 1273 K and 2273 K , but the samples used here were all produced by hot pressing at 1973 K with a dwell time of 60 minutes to yield a porosity of approximately 40%. The applied pressure was gradually increased to 12 MPa and maintained for 15 minutes at each sintering temperature. After cooling, the graphite paper was removed by grinding.

An overview of the tested samples is given in Table 1. In total, twelve samples were tested. A layer of residue – formed by locally densified powder particles – could be observed on the surfaces of some of the partially sintered

Table 1 UHTC sample overview.

| Sample ID | Porosity, ϕ [%] | D [mm] | L [mm] | Type | Treatments | Batch number |
|-----------|----------------------|----------|----------|--------------------|---------------------------|--------------|
| UHTC-2 | 42 | 70 | 5 | partially sintered | abrasion | 1 |
| UHTC-3 | 41 | 70 | 5 | partially sintered | abrasion | 1 |
| UHTC-4 | 41 | 70 | 5 | partially sintered | abrasion | 1 |
| UHTC-5 | 41 | 80 | 5 | partially sintered | ultrasonic bath | 2 |
| UHTC-6 | 41.1 | 80 | 5 | partially sintered | ultrasonic bath, abrasion | 2 |
| UHTC-7 | 41.6 | 80 | 5 | partially sintered | ultrasonic bath | 2 |
| UHTC-8 | 40.9 | 80 | 5 | partially sintered | ultrasonic bath | 2 |
| UHTC-9 | 32.5 | 80 | 5 | partially sintered | ultrasonic bath | 3 |
| UHTC-10 | 31.6 | 80 | 5 | partially sintered | ultrasonic bath | 3 |
| UHTC-11 | 32.6 | 80 | 5 | partially sintered | ultrasonic bath | 4 |
| UHTC-12 | 39.5 | 80 | 5 | partially sintered | ultrasonic bath | 4 |
| UHTC-13 | 34.6 | 80 | 5 | partially sintered | ultrasonic bath | 4 |

**Fig. 3** ZrB₂ porous sample: (a) 70 mm diameter samples with 5 mm thickness, (b) a scanning electron microscopy (SEM) micrograph of the microstructure of a sample, and (c) a sample machined with EDM.

samples, and therefore it was decided to abrade the surfaces with sandpaper by hand. Subsequently, samples UHTC-2, UHTC-3, and UHTC-4 were tested for their permeability characteristics before and after sanding the surface with sandpaper. The next batches of samples, i.e. UHTC-5 to UHTC-13, were treated in an ultrasonic bath to get rid of the residue, and to verify the effectiveness of the ultrasonic bath, permeability tests were performed on UHTC-6 before and after sanding. After completing the permeability tests, all samples were machined with Electrical Discharge Machining (EDM) into a disc form of $\varnothing 60 \text{ mm} \times 3 \text{ mm}$ with an extrude of $39.5 \text{ mm} \times 39.5 \text{ mm} \times 2 \text{ mm}$ (see Fig. 3c) for the outflow experiments.

III. Darcy-Forchheimer Permeability Test

The pressure drop across a porous medium is governed by the Darcy-Forchheimer equation [23], expressed in differential form as

$$-\frac{dp}{dx} = \underbrace{\frac{\mu}{K_D} v}_{\text{viscous term}} + \underbrace{\frac{\rho}{K_F} v^2}_{\text{kinetic term}}. \quad (1)$$

Here, K_D and K_F are material intrinsic permeability coefficients respectively known as the Darcy coefficient and the Forchheimer coefficient; v is the superficial velocity of the flowing medium (also known as the bulk velocity). The left-hand-side of Eq.(1) stands for the pressure gradient across the porous medium, whereas the two terms on the right-hand-side denote the viscous and kinetic losses, respectively. At very low velocities, the kinetic term is negligible and the flow is in the Darcy regime. In this case, the kinetic term of Eq.(1) is left out and the equation becomes the Darcy equation. However, at higher velocities, the kinetic term dominates and the flow enters the Forchheimer regime, requiring the full Darcy-Forchheimer equation.

Equation 1 is integrated by separation of variables over the thickness, L , and from p_{in} to p_{out} as

$$-\int_{p_{in}}^{p_{out}} p dp = \int_0^L \left(\frac{\mu \dot{m} RT}{K_D A} + \frac{\dot{m}^2 RT}{K_F A^2} \right) dx \dots \left[\because v = \frac{\dot{m} RT}{p A} \text{ (continuity)} \right],$$

where \dot{m} is the mass flow rate through area A and R is the specific gas constant. With a constant temperature assumption, $T = T_{in}$, in the whole porous domain, the integration yields the following equation:

$$\frac{p_{in}^2 - p_{out}^2}{2} = \frac{\mu(T_{in}) \dot{m} RT_{in}}{K_D A} L + \frac{\dot{m}^2 RT_{in}}{K_F A^2} L$$

Finally, substitution by $v_{in} = \frac{\dot{m} RT_{in}}{p A}$ and $\rho_{in} = \frac{p_{in}}{RT_{in}}$ yields the Darcy-Forchheimer equation in its integrated form:

$$\frac{p_{in}^2 - p_{out}^2}{2 p_{in} L} = \frac{\mu(T_{in})}{K_D} v_{in} + \frac{\rho_{in}(p_{in}, T_{in})}{K_F} v_{in}^2. \quad (2)$$

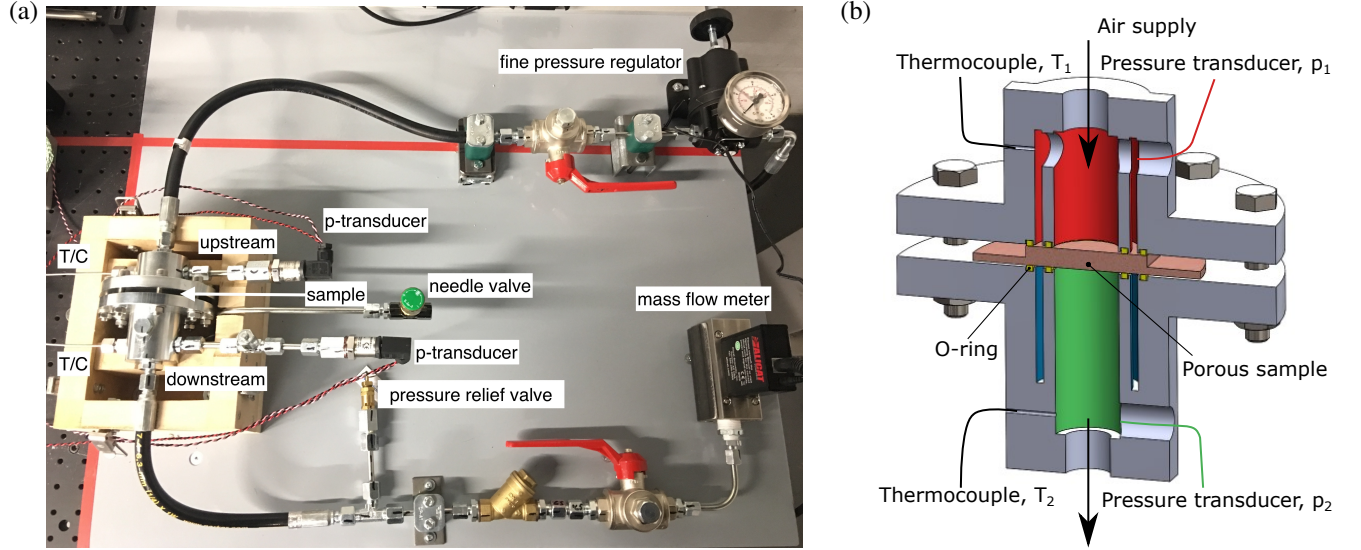


Fig. 4 (a) Darcy-Forchheimer ISO 4022 Permeability Test Rig and (b) a cutaway of the clamping body including its instrumentation.

Here, the subscripts ‘*in*’ and ‘*out*’ respectively denote input and output quantities. The normalised differential pressure, $\frac{p_{in}^2 - p_{out}^2}{2p_{in}L}$, is henceforth expressed as $\frac{\Delta p}{L}$. Since the dynamic viscosity – calculated from Sutherland’s law [24] – and the density – obtained from the ideal gas law – of the fluid are functions of temperature, a modified version of Eq.(2) proposed by Langener et al. [13] can be used in the case of a thermal gradient in the material. However, Eq.(2) is sufficient for the purpose of this paper as the temperature non-uniformity is negligible for the conducted experiments.

A. Permeability Test Rig

In order to determine the permeability coefficients, a test rig has been designed and built in accordance with the ISO 4022 standard [21]. The porous sample is clamped between the upstream and downstream parts as shown in Fig. 4a. A K-type thermocouple (T/C) and a pressure transducer (Gems 3100 Series) are fitted to either part; these record the values of $T_1 = T_{in}$, $T_2 = T_{out}$, $p_1 = p_{in}$, and $p_2 = p_{out}$ (see Fig. 4b). During a test, the input pressure is increased in steps using a fine-adjustment pressure regulator (Fairchild 10292H). Adhering to the ISO 4022 standard, the mass flow rate is measured at a downstream location (Alicat M Series mass flow meter). The through-flow area for this rig is $A = 1.911 \times 10^{-4} \text{ m}^2$ (through-flow diameter of 15.6 mm).

A gradient-free optimisation method proposed by Nelder & Mead [25] is employed to obtain the permeability coefficients, K_D and K_F . The minimisation criterion for this simplex search solution is given by

$$f(\vec{K}) = \frac{\left\| \frac{\Delta p}{L} \Big|_{DF} - \frac{\Delta p}{L} \Big|_{exp} \right\|}{\left\| \frac{\Delta p}{L} \Big|_{exp} \right\|}, \quad (3)$$

where $\vec{K} = [K_D \ K_F]^T$. Here, $\frac{\Delta p}{L}\bigg|_{\text{exp}}$ is obtained from the experimental data points, $\frac{\Delta p}{L}\bigg|_{\text{DF}}$ is given by the right-hand-side of Eq.(2), and the symbol $\|\cdot\|$ denotes the euclidean norm. For a two-dimensional space, the Nelder-Mead algorithm employs three points and – for each iteration – picks the best point that satisfies $f = f_{\min}$. Per iteration, j , the three points are updated by reflection, outside/inside contraction, and shrinking until the conditions $|f^{(j+1)} - f^{(j)}| \leq \epsilon$ and $|\vec{K}^{(j+1)} - \vec{K}^{(j)}| \leq \epsilon$ both are fulfilled. A termination tolerance of $\epsilon = 1 \times 10^{-10}$ is selected here.

B. Validation

In order to validate the results obtained from the permeability test rig, a porous disc of sintered bronze (SIKA-B 8: 89% Cu + 11% Sn) (see Fig. 5a) provided by GKN Sinter Metals Filters GmbH was tested. The experimentally obtained permeability coefficients along with the permeability coefficients stated on the manufacturer's data sheet (Filter-Elements, [26]) for SIKA-B 8 are given in Table 2. The corresponding test results are illustrated in Fig. 5d.

Whilst the Darcy coefficient obtained from the experiment is in close agreement with that from the data sheet, the Forchheimer coefficient is lower by a factor of approx. 5. In Fig. 5d, it can be seen that the normalised differential pressure (blue dot-dashed line) obtained from Eq.(2) using the coefficients from the data sheet under-predicts the pressure loss across the medium in comparison to the experimental data as the superficial input velocity increases. This is due to the fact that the manufacturer performed the permeability tests at very low differential pressures [26] where the flow was dominated by the Darcy component, and thus the test did not capture a representative Forchheimer coefficient. Hence, despite matching the Darcy coefficient with a discrepancy of only 7.5%, a different approach to validating the rig was required to account for the flow in the Forchheimer regime.

Several correlations exist for predicting the pressure loss across a porous material that is composed of a packed bed. Erdim et al. [27] reviewed and evaluated 38 correlations from the literature. The most widely used correlation for a packed bed of spherical, mono-sized particles was proposed by Ergun [28], where the Darcy and Forchheimer coefficients were respectively proposed as

$$K_{D, \text{Ergun}} = \frac{\phi^3 d_p^2}{150(1 - \phi)^2} \quad (4)$$

Table 2 Permeability coefficients of SIKA-B 8.

| Source | K_D [10^{-12} m ²] | K_F [10^{-6} m] |
|---|-------------------------------------|----------------------|
| ISO 4022 experiment | 2.162 | 1.023 |
| SIKA-B data sheet (Filter-Elements, [26]) | 2 | 5.2 |
| Ergun approximation | 1.971 | 1.623 |

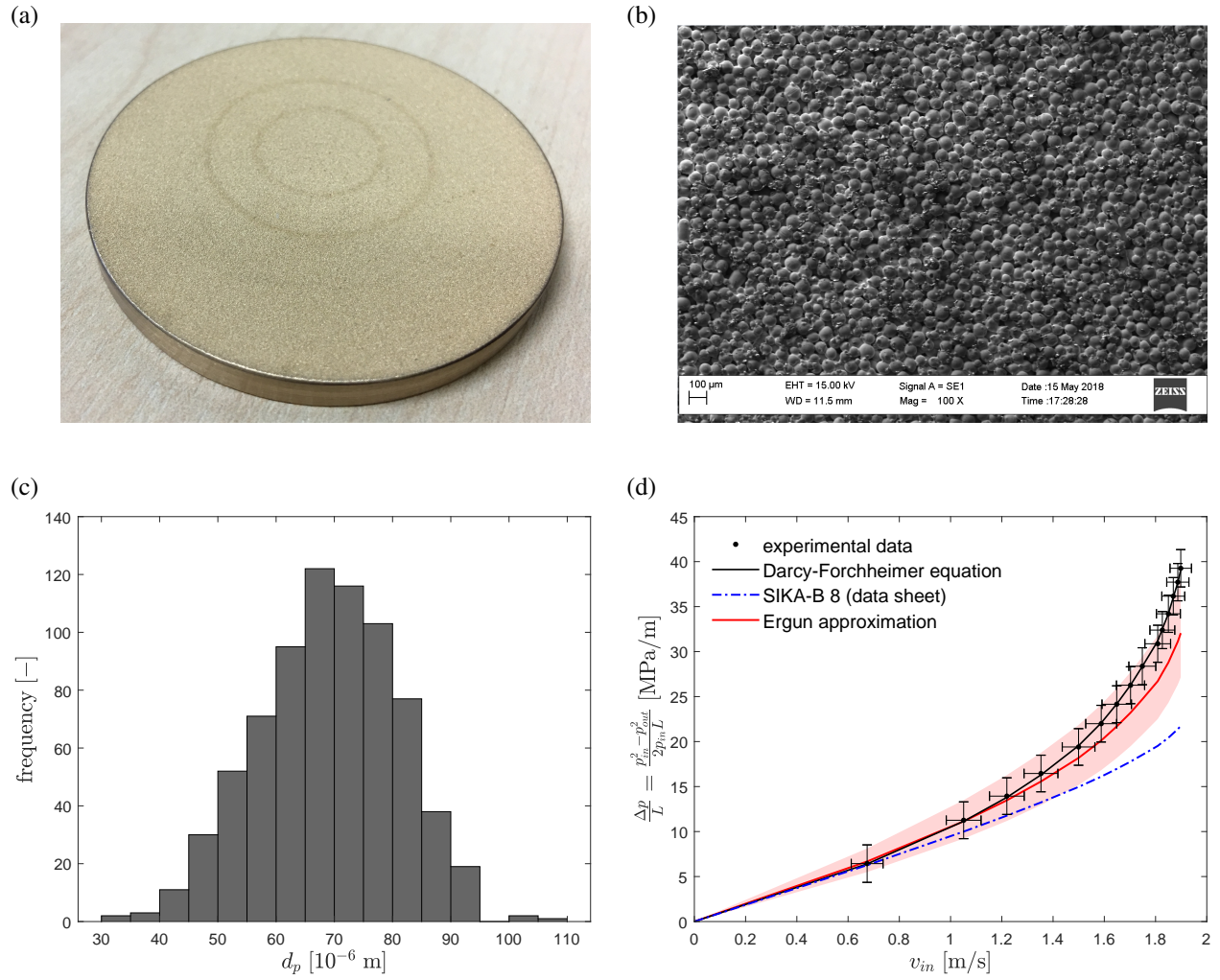


Fig. 5 (a) SIKA-B 8 ($\varnothing 60$ mm \times 5 mm), (b) SEM image of SIKA-B 8 at $\times 100$ magnification (courtesy: Dr Elsiddig Elmukashfi), (c) histogram of the diameter of 742 particles of SIKA-B 8, and (d) normalised differential pressure versus superficial input velocity of SIKA-B 8 (the light-red band represents the uncertainty in Ergun approximation, i.e. in Eq.(4) and Eq.(5).

and

$$K_{F, \text{Ergun}} = \frac{\phi^3 d_p}{1.75(1 - \phi)}. \quad (5)$$

Here, d_p is the diameter of the particles in the packed bed and ϕ is the porosity of the material. Since the SIKA-B 8 sample is made of regular spherical particles [26], these correlations are appropriate for modelling the flow through it. SEM images (see Fig. 5b) of either surface of a single SIKA-B 8 disc were taken to measure the particle diameter, where the scale on the SEM images was taken as the reference. The measured diameter, d_p , of $n_p = 742$ particles yielded a distribution shown in Fig. 5c with a mean of $\bar{d}_p = 68.935 \times 10^{-6}$ m and a standard deviation of $\sigma_{d_p} = 11.764 \times 10^{-6}$ m. Furthermore, a density based measurement – comparing the weight of this sample to the theoretical weight of a fully dense one of identical volume – determined a porosity of $\phi = 30.1\%$.

Since the diameter is a distribution, rather than a single value, the normalised differential pressure was evaluated at the Sauter mean diameter [29], $d_p = d_{32}$, to approximate the Ergun correlation (henceforth annotated as ‘Ergun approximation’, e.g. in Fig. 5d). The Sauter mean diameter is defined as

$$d_{32} = \frac{\sum \bar{d}_{p,i}^3 f_i}{\sum \bar{d}_{p,i}^2 f_i}, \quad (6)$$

where $\bar{d}_{p,i}$ denotes the average diameter within the i -th bin in the histogram and f_i refers to the corresponding frequency or count. The Sauter mean diameter represents the equivalent spherical diameter that has the same effective surface of that in the entire distribution. The calculated permeability coefficients from Eq.(4) and Eq.(5) using the Sauter diameter, $d_p = d_{32}$, are given in Table 2 (Ergun approximation). The pressure loss obtained from the Ergun approximation (solid, red line) is plotted in Fig. 5d. The light-red band represents the uncertainty in the Ergun approximation, i.e. in Eq.(4) and Eq.(5), which was obtained by employing Moffat’s error propagation method described in Appendix A. The individual error in the diameter, δd_p , was estimated as a systematic bias uncertainty [30] in measuring the diameter of the spheres from SEM images. This was estimated to be equivalent to two pixels and equal for all measurements. The relative uncertainty in the porosity, $\frac{\delta \phi}{\phi}$, was estimated to be $\pm 3\%$.

Fig. 5d demonstrates a good agreement between the experimentally measured pressure drop and the Ergun approximation. At higher velocities, however, there is a slight divergence. This is reflected in the permeability coefficients as well (Table 2). The experimentally obtained value for K_D matches the one calculated from the Ergun approximation within 9.7%, whereas the K_F value differs by 37%. For reference, the uncertainty in the experimentally measured value is 12% for K_D as well as for K_F . The discrepancy in K_F can be attributed to the wide particle size distribution in SIKA-B 8. Keyser et al. [31] and Koekemoer & Luckos [32] showed in separate studies that the Ergun correlation evaluated at the Sauter mean diameter under-predicts the pressure loss when the particle size distribution is wide. This trend is evident in the present case. However, the Ergun approximation under-predicts the experimentally

measured pressure drop by only up to 18% within the tested velocity range. This difference is within the $\pm 50\%$ prediction accuracy reported by Macdonald et al. [33] for such correlations.

Overall, the experimental data and the Ergun approximation, along with their respective uncertainties, are in good agreement. The measured values of the permeability coefficients, K_D and K_F , are close to that obtained by the Ergun approximation, and the associated discrepancies are within the range reported in the literature. The validation is thereby concluded.

C. Results and Discussion

The permeability coefficients for all twelve UHTC samples yielded from the Nelder-Mead simplex search solution are given in Table 3 along with their respective uncertainties. A *Monte Carlo* simulation was performed to determine the uncertainties (see Appendix A for details). For the tested samples, the order of the Darcy coefficient ranges from 10^{-15} m^2 to 10^{-14} m^2 and the Forchheimer coefficient from 10^{-9} m to 10^{-7} m . The through-flow results are showcased in Fig. 6 for UHTC-3 (post-sand). The normalised differential pressure is plotted against the superficial input velocity including the uncertainties of the experimental data in form of error bars. The solid line, which represents the Darcy-Forchheimer equation, is obtained by using the K_D and K_F values in Eq.(2). In Fig. 6, it can be observed that the experimental data follow the Darcy-Forchheimer equation, which is within the uncertainties. At lower velocities, the curve is fairly linear; however, as the velocity rises, the non-linearity of the curve becomes prominent. Furthermore, it can be seen (Fig. 6) that the flow enters the Forchheimer regime at higher velocities and deviates from the projected Darcy equation significantly as the superficial input velocity rises. At $v_{in} = 0.35 \text{ m/s}$, this discrepancy reaches up to approx. 12%, demonstrating the importance of using the Darcy-Forchheimer equation instead of the Darcy equation for this type of materials at higher through-flow velocities.

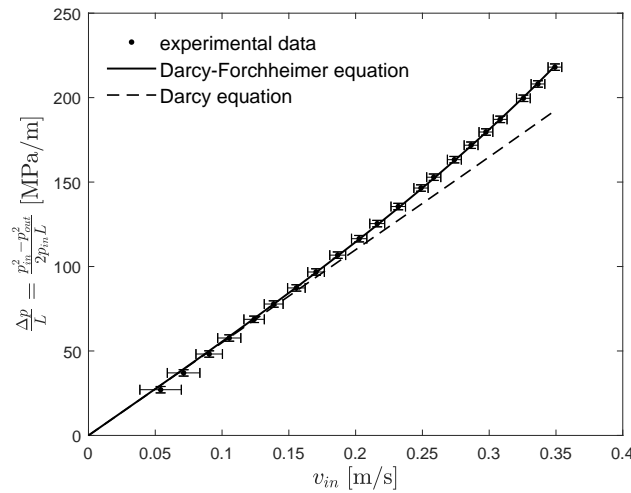


Fig. 6 Results for UHTC-3 (post-sand): normalised differential pressure versus superficial input velocity.

Table 3 Permeability coefficients and their corresponding uncertainties. Note: ‘prs’ and ‘pos’ stand for pre-sand and post-sand, respectively.

| Sample ID | K_D [10^{-14} m ²] | δK_D [10^{-14} m ²] | $\frac{\delta K_D}{K_D}$ [%] | K_F [10^{-7} m] | δK_F [10^{-7} m] | $\frac{\delta K_F}{K_F}$ [%] |
|--------------|-------------------------------------|--|------------------------------|----------------------|-----------------------------|------------------------------|
| UHTC-2 | 2.998 | ±0.055 | ±1.8 | 1.59 | ±0.43 | ±27 |
| UHTC-3 (prs) | 3.107 | ±0.061 | ±2.0 | 1.31 | ±0.31 | ±23 |
| UHTC-3 (pos) | 3.297 | ±0.063 | ±1.9 | 1.26 | ±0.25 | ±20 |
| UHTC-4 (prs) | 0.596 | ±0.047 | ±7.9 | 0.023 | −0.008, +0.015* | −36, +63* |
| UHTC-4 (pos) | 0.912 | ±0.048 | ±5.3 | 0.075 | −0.024, +0.045* | −32, +60* |
| UHTC-5 | 2.956 | ±0.064 | ±2.2 | 1.11 | ±0.29 | ±26 |
| UHTC-6 (prs) | 3.754 | ±0.069 | ±1.8 | 1.70 | ±0.36 | ±21 |
| UHTC-6 (pos) | 3.731 | ±0.073 | ±2.0 | 1.54 | ±0.33 | ±22 |
| UHTC-7 | 3.726 | ±0.061 | ±1.6 | 1.97 | ±0.37 | ±19 |
| UHTC-8 | 3.775 | ±0.067 | ±1.8 | 1.74 | ±0.35 | ±20 |
| UHTC-9 | 0.340 | ±0.027 | ±7.9 | 0.014 | −0.006, +0.008* | −39, +58* |
| UHTC-10 | 0.280 | ±0.024 | ±8.5 | 0.020 | −0.012, +0.038* | −58, +193* |
| UHTC-11 | 0.392 | ±0.027 | ±7.0 | 0.072 | −0.051, +0.361* | −71, +506* |
| UHTC-12 | 1.045 | ±0.037 | ±3.5 | 0.252 | −0.095, +0.20* | −38, +78* |
| UHTC-13 | 0.747 | ±0.026 | ±3.7 | 0.41 | −0.26, +2.2* | −64, +527* |

* The large uncertainties in K_F result in an asymmetric distribution.

The effect of sanding on the overall permeability behaviour is presented in Fig. 7. Upon sanding, the samples demonstrated a clear improvement in their permeability, which is shown in Fig. 7 (UHTC-3 and UHTC-4). The Darcy coefficient increased by 6.1% for UHTC-3 and 19% for UHTC-4 (values obtained from Table 3), which are outside the uncertainty bounds of 2.0% and 7.9%, respectively. For a given differential pressure, this translates into a rise in velocity by up to approx. 5% and 60% respectively for UHTC-3 and UHTC-4. Although the overall permeability is increased by sanding off the surface, there is a possibility that the residual grains from the process block the pores to some extent. This effect however was not possible to account for with the current experimental setup and processes; instead, the next batches of samples, i.e. UHTC-5 to UHTC-13, were treated in an ultrasonic bath. The effectiveness of the ultrasonic bath is demonstrated in Fig. 7 (UHTC-6), where the permeability test was performed before and after sanding. Overall, the data sets taken before and after sanding fall atop each other. The change in the Darcy coefficient here is 0.6%, which is within its uncertainty of 1.8% (see Table 3). This proves the ultrasonic bath to be effective, and therefore the sanding process is not necessary.

A comparison amongst all the twelve UHTC samples in terms of their permeability characteristics is illustrated in Fig. 8. Here, it can be observed that, for a given differential pressure, the permitted flow through can vary by an order of magnitude across the different batches (Table 1), e.g. for a given normalised differential pressure, $\frac{\Delta p}{L} = 200$ MPa/m, the through-flow velocity ranges between $v_{in} = 0.025$ m/s and $v_{in} = 0.4$ m/s. This is because the permeability coefficients

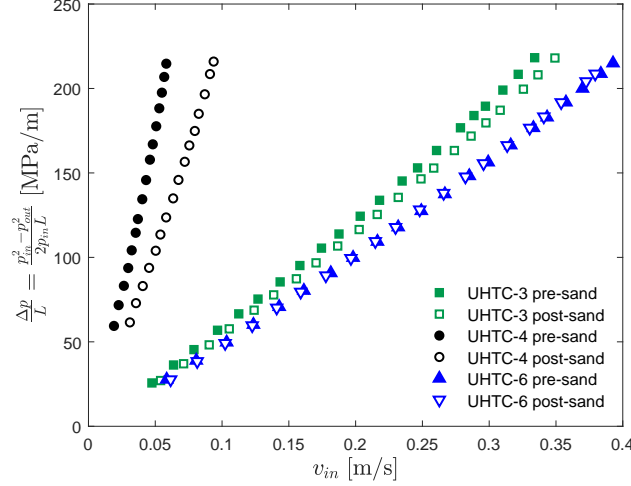


Fig. 7 Sanding effect on the permeability characteristics of (a) samples (UHTC-3 and UHTC-4) not treated in an ultrasonic bath (black and green) and a sample (UHTC-6) treated in an ultrasonic bath (blue).

vary by an order of magnitude in comparison (Table 3). The variation in these coefficients can be attributed to the corresponding porosities (Table 1). This relationship between the porosity and permeability coefficients is visualised in Fig. 9. Although some outliers exist (UHTC-4 in batch 1 and UHTC-11 in batch 4), the general trend shows that an increase in porosity from $\phi \approx 32\%$ to $\phi \approx 42\%$ results in an order of magnitude rise in the Darcy coefficient, K_D (Fig. 9a), and in contrast, two orders of magnitude in the Forchheimer coefficient, K_F (Fig. 9b).

Furthermore, it can be seen that within the first batch of samples (batch 1), i.e. UHTC-2 to UHTC-4, that were not treated in an ultrasonic bath but were sanded, UHTC-4 is an outlier and the rest are fairly similar in terms of their superficial velocity (see Fig. 8) and permeability coefficients (see Table 3). Analogous to batch 1, there is an outlier, i.e. UHTC-5, in batch 2, where the rest of the samples demonstrate a similar behaviour in terms of permeability. The deviation, however, is less compared to the first batch, and the data obtained from samples UHTC-6, UHTC-7, and UHTC-8 overlap fairly well. Moreover, the slight deviation in their permeability coefficients falls within the respective uncertainties – indicating the effectiveness of the ultrasonic bath and the uniformity amongst these UHTCs. In contrast, the outliers, UHTC-4 and UHTC-5, suggest that there are occasional non-uniformities within these samples, and emphasise the need for running the permeability test for each individual sample even if they are manufactured with the same conditions. Batch 4 also demonstrates irregularities. These non-uniformities could occur from locally closed pores, i.e. increased amount of closed porosity, or local patches of more densified material. In addition, it is worth noting that the through-flow took place covering an area of $A = 1.911 \times 10^{-4} \text{ m}^2$, which is approx. 4–5% of the total surface area of the entire sample, depending on the sample’s diameter. This means that not all local non-uniformities are captured within this permeability test.

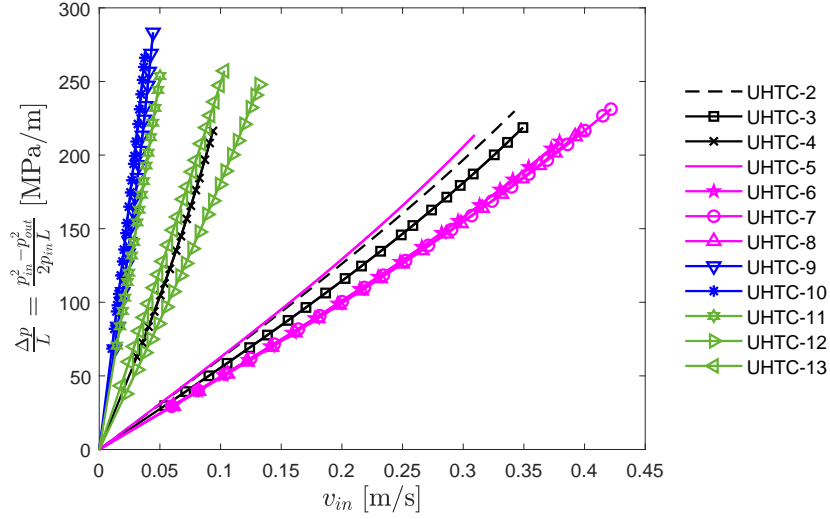


Fig. 8 Comparison amongst all samples: normalised differential pressure versus superficial input velocity. Note: only post-sand data are presented, where applicable. Each batch is represented with a single colour; black: batch 1, magenta: batch 2, blue: batch 3, and green: batch 4.

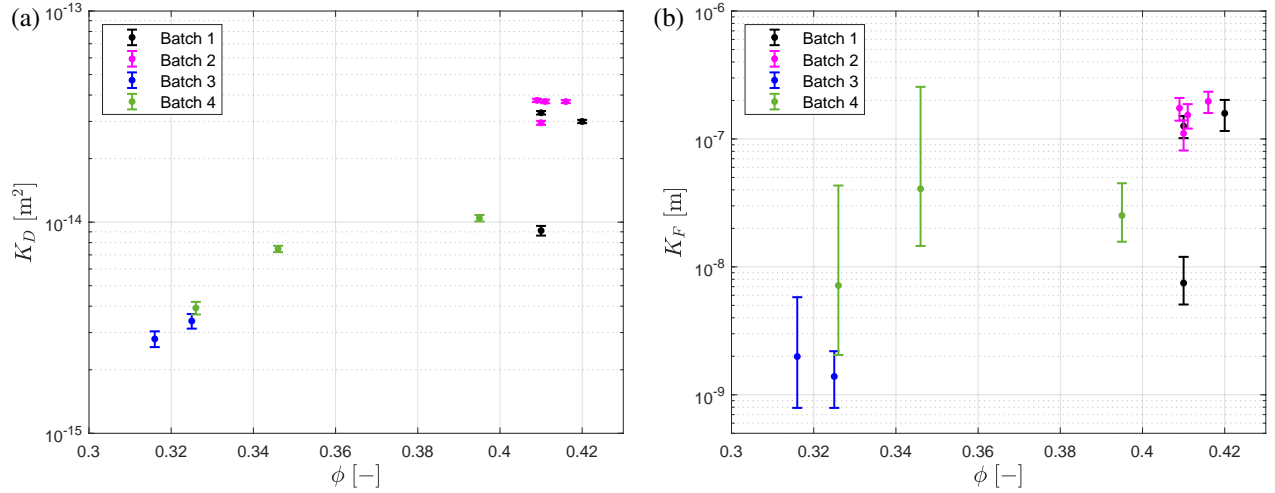


Fig. 9 Permeability coefficients versus porosity: (a) Darcy coefficient and (b) Forchheimer coefficient. Note: only post-sand data are presented, where applicable. Each batch is represented with a single colour.

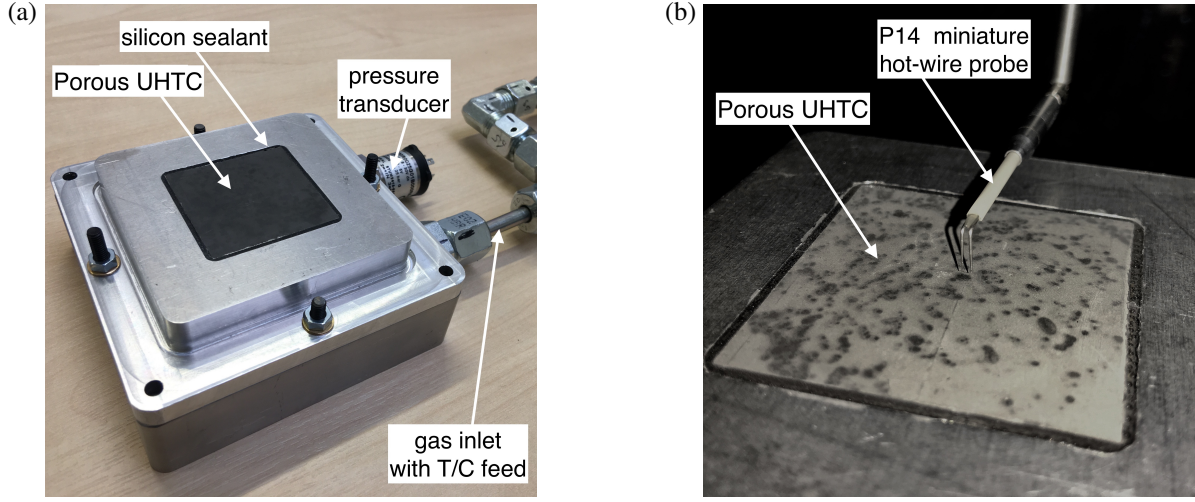


Fig. 10 (a) A UHTC sample attached to the plenum and (b) a miniature hot-wire probe, P14, in operation.

IV. Outflow Experiments

As discussed in the previous section, the UHTC samples can feature irregularities even within a single batch. This indicates that the outflow of these samples could behave in an irregular fashion as well. Therefore, it is necessary to measure the outflow velocity distribution of each sample manufactured in the current process, particularly before employing it in wind tunnel experiments. In order to examine the specially-resolved outflow characteristics of transpiring UHTCs, a bench-top rig has been designed, where the outflow velocity can be mapped and visualised using hot-wire anemometry. In this paper, the outflow behaviour of UHTC-7 and UHTC-8 are characterised.

A. Setup

A machined UHTC sample (see Fig. 3c) is glued and sealed onto a cover-plate by silicon, and subsequently the cover-plate is attached to a plenum that is fitted with a pressure transducer (Gems 3100 Series) and a gas inlet as shown in Fig. 10a. A K-type thermocouple is fed through the gas inlet. The plenum is located atop a set of motorised traverses (Thorlabs MTS50/M-Z8) that move in orthogonal directions with respect to each other. This allows for the sample to be traversed in a two-dimensional plane, $x - y$.

Due to the fine porous structures of the UHTCs, a miniature hot-wire probe is employed (Dantec Dynamics P14; wire dimensions: $5 \mu\text{m}$ in diameter, 1.25 mm in length). The hot-wire anemometry is run in CTA (Constant Temperature Anemometry) mode [34, 35]. During operation, the hot-wire probe is attached to a stationary support and the plenum is traversed at a pre-defined step-size on either direction (see Fig. 10b). The height of the probe from the sample's surface, z , is adjusted by a fine translation stage (Thorlabs DTS50/M).

The choice of the calibrator is of particular importance as the velocities involved in this experiment are low. The probe is calibrated with Dantec's *StreamLine Pro Automatic Calibrator*, which is capable of a wide velocity range, i.e.

0.02 m/s to > 300 m/s, that includes a sufficiently low velocity regime. The collected calibration data are fitted with King's law [34, 35], which is expressed as

$$E^2 = A + Bv^n, \quad 0.4 \leq n \leq 1.0. \quad (7)$$

Here, E and v are the voltage acquired from the CTA and the corresponding velocity is set on the calibrator. The regression coefficients are $A = 1.688$, $B = 0.6203$, and $n = 0.8708$. The exponent's value of $n = 0.8708$ is within the range for low-velocity calibrations reported by Aydin & Leutheusser [36] and Tsanis [37], i.e. $n \approx 0.6 - 1.0$. The calibration curve is plotted in Fig. 11 along with the prediction interval of this fit.

Since ZrB_2 is thermally conductive, the near-wall effect of hot-wires [38] needs to be taken into account. Measurements taken below the height of $z = 3$ mm experience this effect as shown in Fig. 12, where the flow velocity is zero. A correction to account for this is performed as $E_{\text{corr}}^2 = E(z)^2 - E_0^2$, where $E(z)$ is the voltage at a given probe height z and E_0 is the nominal voltage away from the wall, which is constructed by taking the average of the values lying on the asymptote (dashed line in Fig. 12).

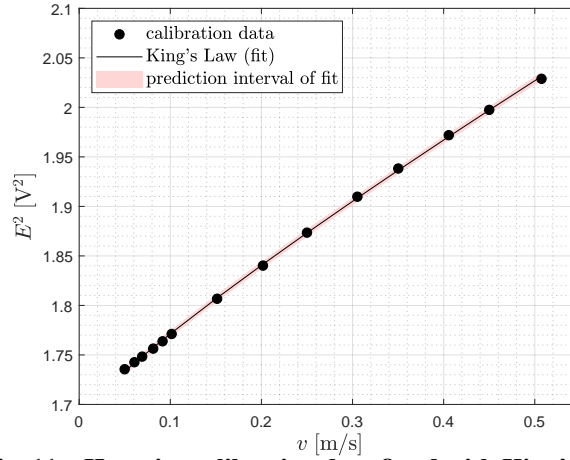


Fig. 11 Hot-wire calibration data fitted with King's Law ($R^2 = 0.99$).

For each run, an area of $43 \text{ mm} \times 43 \text{ mm}$ is covered with a step-size of $1 \text{ mm} \times 1 \text{ mm}$. This covers the through-flow area of $39.5 \text{ mm} \times 39.5 \text{ mm}$. The plenum pressure, p_{plenum} , plenum temperature, T_{plenum} , and hot-wire data are acquired for each step. The overall process takes about 3.5 hours to complete and the plenum pressure fluctuates slightly over time, which leads to minor discrepancies in the velocity across the sample. Hence, the measured velocity from the hot-wire, v_{hw} , at each cell is normalised as

$$\bar{v}_{out} = \frac{v_{hw}}{v_{out}}, \quad (8)$$

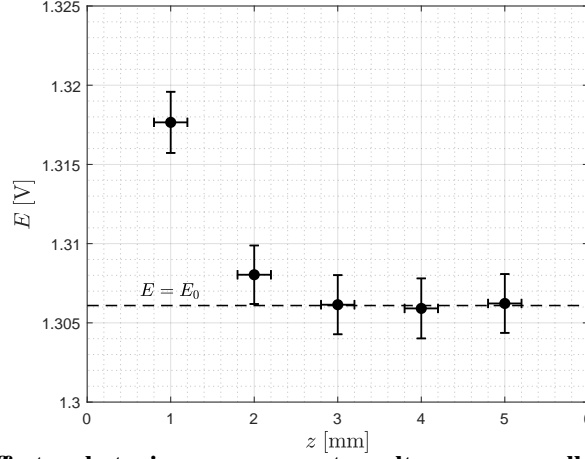


Fig. 12 Near-wall effect on hot-wire measurements: voltage versus wall-normal distance. Note: the error bar for voltage is obtained from the standard deviation and an estimated uncertainty of $\Delta z = \pm 0.2$ mm is plotted for distance.

where v_{out} is the superficial output velocity obtained from the Darcy-Forchheimer equation

$$\frac{p_{in}^2 - p_{out}^2}{2p_{out}L} = \frac{\mu(T_{out})}{K_D}v_{out} + \frac{\rho_{out}(p_{out}, T_{out})}{K_F}v_{out}^2, \quad (9)$$

expressed in terms of output quantities. Here, the input and output conditions correspond to the plenum and atmospheric conditions, respectively, for each measurement location. The non-dimensional output velocity, \bar{v}_{out} , therefore incorporates the fluctuations in the plenum pressure and also shows how close the obtained velocity is compared to the theoretical Darcy-Forchheimer velocity, e.g. it would be equal at unity, i.e. $\bar{v}_{out} = 1$. This also serves as a baseline quantity to compare the uniformity of a particular measurement location with its neighbouring ones.

B. Results and Discussion

The outflow results obtained from the hot-wire anemometry are presented in Fig. 13. Figures 13c and 13d show the outflow maps in terms of the non-dimensional output velocity, \bar{v}_{out} , for UHTC-7 and UHTC-8, respectively. The corresponding histograms are shown in Figs. 13e and 13f. Reference images of UHTC-7 and UHTC-8 are respectively embedded in Figs. 13a and 13b. The plenum pressure was set at $p_{plenum} = 4$ bar (g) with air as the injected gas. The hot-wire probe was set at a height of $z = 2$ mm. In Table 4, the mean velocity measured by the hot-wire probe, \bar{v}_{hw} ,

Table 4 Comparison between velocities obtained from hot-wire anemometry and mass flow meter.

| Sample ID | $\bar{v}_{hw} \pm \delta\bar{v}_{hw}$ [m/s] | $\frac{\delta\bar{v}_{hw}}{\bar{v}_{hw}}$ [%] | $v_{\dot{m}} \pm \delta v_{\dot{m}}$ [m/s] | $\frac{\delta v_{\dot{m}}}{v_{\dot{m}}}$ [%] |
|-----------|---|---|--|--|
| UHTC-7 | 0.481 ± 0.012 | 2.50 | 0.447 ± 0.046 | 10.2 |
| UHTC-8 | 0.433 ± 0.012 | 2.77 | 0.409 ± 0.042 | 10.3 |

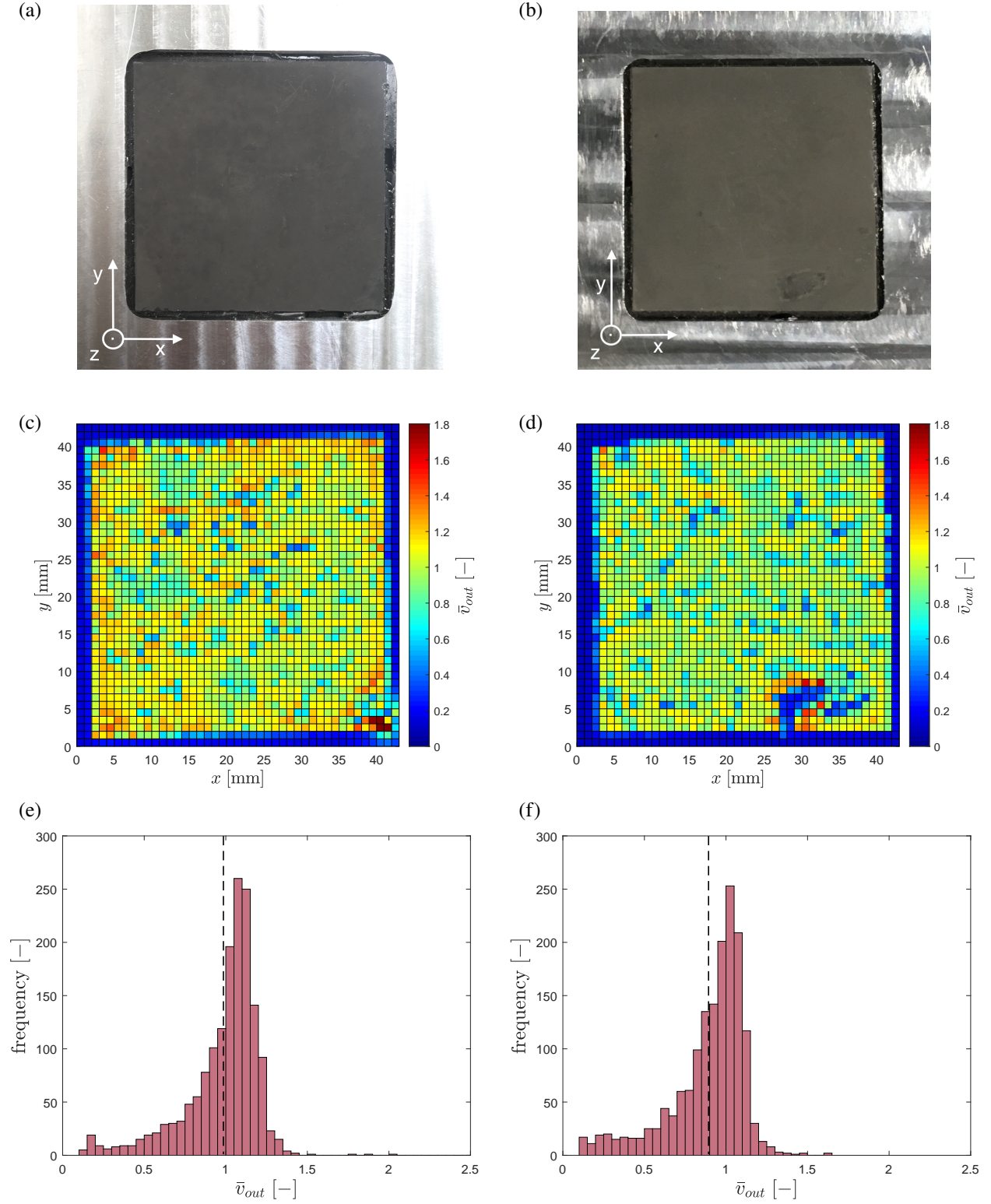


Fig. 13 Reference frame for traversing: (a) UHTC-7 and (b) UHTC-8; outflow map in terms of the non-dimensional output velocity, \bar{v}_{out} : (c) UHTC-7 and (d) UHTC-8; and histogram of \bar{v}_{out} : (e) UHTC-7 and (f) UHTC-8 (the dashed line represents the mean value). The injected gas is air at $p_{plenum} = 4$ bar (g). Height of the probe is at $z = 2$ mm.

is compared against the velocity obtained from the mass flow meter, v_{in} , for both samples. The mean velocity from hot-wire anemometry is in close agreement with the mass flow meter's velocity for both UHTC-7 and UHTC-8. The discrepancy between the two measurement sources is 7.6% for UHTC-7 and 5.9% for UHTC-8, which are within the uncertainty in v_{in} (Table 4). This validates the overall hot-wire velocity measurement, especially the performed calibration at these low speeds and the wall correction.

Figures 13c and 13d demonstrate a fairly uniform velocity distribution across the samples. The contour level in terms of the non-dimensional output velocity, \bar{v}_{out} , is close to 1 over the majority of the outflow region. This is further evident in the corresponding histograms in Figs. 13e and 13f. The mean value, represented by the dashed line, is close to 1 for both samples, which demonstrates that the obtained spatial measurements largely adhere to the theoretical value calculated by the Darcy-Forchheimer equation. The standard deviations are 0.24 (UHTC-7) and 0.23 (UHTC-8), which respectively correspond to 24.4% and 25.8% on the mean value (average of the two: 25.1%). Most importantly, the velocity varies within the same order of magnitude, which suggests that unwanted jets are absent. There is a small region of approximately twice the mean velocity on the bottom-right corner of UHTC-7 (Fig. 13c). This could be due to a small leakage or a more permeable zone locally. On UHTC-8, there is a small area where no outflow is present (from $x = 27$ mm to $x = 39$ mm and $y = 2$ mm to $y = 9$ mm, 13d). This is a densified region that can be seen on the sample itself in Fig. 13b. Apart from these outlying regions, both samples show a regular flow-field with practically no blockage.

Overall, the outflow of these UHTCs exhibits a good uniformity. As there is no individual jet or large blockages, the coolant mass can be injected in a fairly uniform fashion into the boundary-layer for the purpose of transpiration cooling. However, the outflow characteristics of two different samples are not identical, and large variations could exist in the current manufacturing process. It is therefore necessary to characterise the outflow of each sample before use. These velocity maps could be used as a boundary condition in numerical modelling and as a reference to interpret the mass flow distribution in wind tunnel experiments.

V. Conclusion

The permeability and outflow behaviour of porous Ultra-High-Temperature-Ceramics (UHTC) made of ZrB_2 were experimentally examined to assess their suitability for transpiration cooling, a thermal protection system that could enhance the re-usability of hypersonic vehicles such as rockets and spaceplanes. It is shown that the flow through these UHTCs can be successfully modelled by the Darcy-Forchheimer equation even at higher through-flow velocities, and the corresponding permeability coefficients are measured in an ISO 4022 rig featuring a through-flow diameter of 15.6 mm and reported along with their respective uncertainties. A change in porosity, from $\phi \approx 32\%$ to $\phi \approx 42\%$, results in an order of magnitude jump in the Darcy coefficient, whereas the Forchheimer coefficient increases by two orders of magnitude, approximately. Cleaning the surface of the porous samples – in form of sanding or ultrasonic bath – increased the Darcy coefficient by up to 19%. Velocity maps obtained from hot-wire anemometry demonstrate good

outflow characteristics that behave in a uniform fashion. The standard deviation of the velocity distribution is 25.1% with respect to the mean value. No individual jets are present. The results published here can be used in numerical modelling and experimental design of wind tunnel testing, where porous injectors made of UHTC are involved. Furthermore, the permeability coefficients could help designers predict the coolant mass budget for vehicles that will feature transpiration cooling. Whilst the brittleness of porous UHTC restricts its ease of application – in terms of the flow characteristics – it is demonstrably a befitting candidate for transpiration cooling.

Appendix

A. Uncertainty Analysis

The uncertainties in the variables $\frac{\Delta p}{L}$, μv_{in} , and $\rho_{in} v_{in}^2$ were calculated using Moffat's error propagation method [39] defined as

$$\delta X = \sqrt{\sum_{i=1}^N \left(\frac{\partial X}{\partial Y_i} \delta Y_i \right)^2}, \quad (10)$$

where each variable is given as $X = X(Y_1, Y_2, \dots, Y_N)$. Here, X is the variable which is calculated from measurements, Y_i , using data from the experiment. The uncertainties in Y_i , denoted by δY_i , are determined from the uncertainty given by the manufacturer of the employed equipment (see Table 5). In order to find the uncertainties in the permeability coefficients, a Monte Carlo simulation [30] was performed for 1×10^6 events. For this purpose, 1×10^6 random events were created for the aforementioned variables around each experimental data point which followed a Gaussian distribution. The Gaussian distribution was defined by an expected value of $E = X$ and a standard deviation of $\sigma = \frac{\delta X}{2}$. Hence, the uncertainty δX was given by a confidence interval of 95% for each variable, and thus the process 'simulated' 1×10^6 events of the same experiment within the given bounds of uncertainty. Subsequently, the Nelder-Mead simplex search optimisation process was carried out for each event, hence 1×10^6 times, which yielded Gaussian distributions for K_D and K_F . The uncertainties for the permeability coefficients were determined as $\delta K_D = \pm 2\sigma$ and $\delta K_F = \pm 2\sigma$ – and therefore within a confidence interval of 95% – from their respective distributions.

The histograms of K_D and K_F for UHTC-3 (pos) generated from the Monte Carlo simulation are respectively illustrated in Fig. 14a and Fig. 14b, and the corresponding uncertainties in variables $\frac{\Delta p}{L}$, μv_{in} , and $\rho_{in} v_{in}^2$ are shown in

Table 5 Apparatus uncertainties. F.S.O. = full scale output.

| Gauge | Variable | Absolute error [%] | F.S.O. error [%] | F.S.O. | Reading error [%] |
|----------------------------------|-------------------|--------------------|------------------|------------|-------------------|
| Pressure transducer, Gems 3100 | p_{in} | n/a | 0.25 | 40 bar (g) | n/a |
| Pressure transducer, Gems 3100 | p_{out} | n/a | 0.25 | 25 bar (g) | n/a |
| Thermocouple, K-type | T_{in}, T_{out} | 0.5 K | n/a | n/a | n/a |
| Mass flow meter, Alicat M Series | \dot{m} | n/a | 0.2 | 250 slpm | 0.8 |

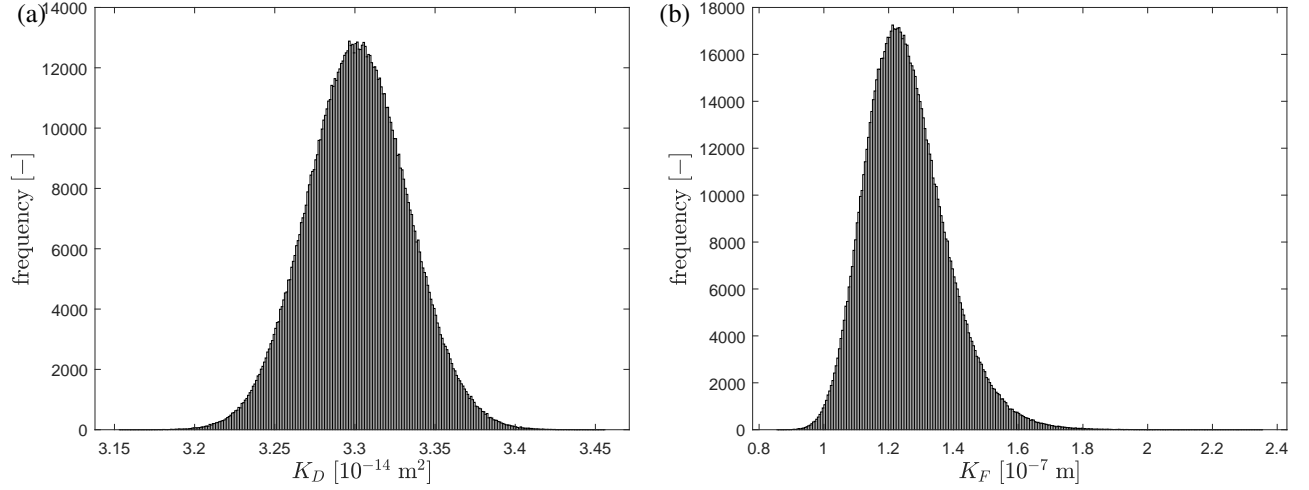


Fig. 14 Histogram of (a) K_D and (b) K_F for 1×10^6 events obtained from the Monte Carlo Simulation. Sample: UHTC-3 (pos).

Fig. 15a. For cases where the uncertainties in the permeability coefficients are high, the Monte Carlo simulation yields an asymmetric distribution. The uncertainties for the coefficients within a confidence interval of 95% is calculated from a probabilistically symmetric distribution according to Coleman & Steele [30] after filtering out any value that is equal or larger than unity. A histogram of such a case (UHTC-4) is presented in Fig. 15b.

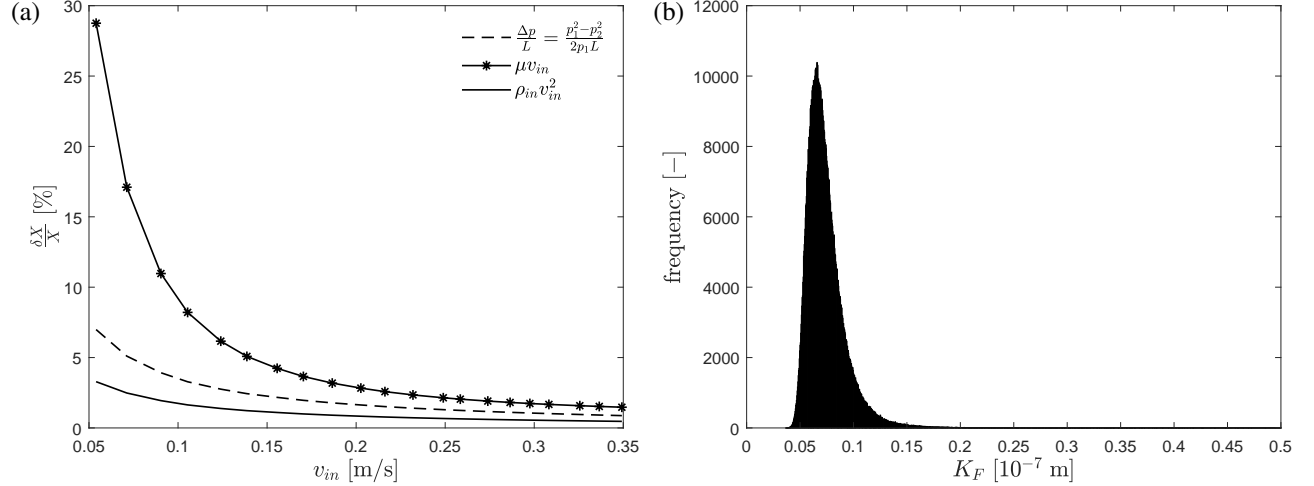


Fig. 15 (a) Uncertainties of different variables for each data point with respect to their corresponding superficial input velocity and (b) asymmetric histogram of K_F obtained from the Monte Carlo Simulation; sample: UHTC-4 (pos).

Acknowledgements

The funding for this research by the EPSRC grant ‘Transpiration Cooling Systems for Jet Engine Turbines and Hypersonic Flight’ (reference: EP/P000878/1) is duly acknowledged. The authors of this paper would like to thank the following people: Professor Peter Ireland, Professor David Gillespie, Professor Luca Di Mare, and Jack Lavender for

their contribution to the design and setup of the experimental rigs; Dr Luke Doherty for his support in performing the uncertainty analysis; Gregory King, William Godfrey, Hal Surtell, and Jason McCluskey for their assistance in building the experimental rigs; Christian Giebel for providing the SIKA-B 8 sample; and Dr Elsiddig Elmukashfi for the SEM images.

References

- [1] van Driest, E. R., “The Problem of Aerodynamic Heating,” *Aeronautical Engineering Review*, 1956, pp. 26–41.
- [2] Anderson, J. J. D., *Hypersonic and High-Temperature Gas Dynamics, Second Edition*, American Institute of Aeronautics and Astronautics, Reston, VA, 2006. <https://doi.org/10.2514/4.861956>.
- [3] Varvill, R., and Bond, A., “The Skylon Space Plane: Progress to Realisation,” *British Interplanetary Science*, Vol. 61, 2008, pp. 412–418.
- [4] Esser, B., Barcena, J., Kuhn, M., Okan, A., Haynes, L., Gianella, S., Ortona, A., Liedtke, V., Francesconi, D., and Tanno, H., “Innovative Thermal Management Concepts and Material Solutions for Future Space Vehicles,” *Journal of Spacecraft and Rockets*, Vol. 53, No. 6, 2016, pp. 1051–1060. <https://doi.org/10.2514/1.A33501>.
- [5] Launius, R. D., and Jenkins, D. R., *Coming Home: Reentry and Recovery from Space*, 2012.
- [6] Tanno, H., Komuro, T., Itoh, K., Kuhn, M., Petkov, I., and Esser, B., “Transpiration cooling experiments in free-piston shock tunnel HIEST,” *th European Workshop on Thermal Protection Systems and Hot Structures*, Noordwijk, Netherlands, 2016.
- [7] Böhrk, H., “Transpiration Cooling at Hypersonic Flight - AKTiV on SHEFEX II,” *11th AIAA/ASME Joint Thermophysics and Heat Transfer Conference*, American Institute of Aeronautics and Astronautics, Reston, Virginia, 2014, p. 175. <https://doi.org/10.2514/6.2014-2676>.
- [8] Ewenz Rocher, M., McGilvray, M., Hermann, T. A., Ifiti, H. S., Hufgard, F., Eberhart, M. F., Meindl, A., Loehle, S., Giovannini, T., and Vandeperre, L. J., “Testing a Transpiration Cooled Zirconium-Di-Boride sample in the Plasma Tunnel at IRS,” *AIAA Scitech 2019 Forum*, American Institute of Aeronautics and Astronautics, Reston, Virginia, 2019, p. 01. <https://doi.org/10.2514/6.2019-1552>.
- [9] Schneider, S. P., “Hypersonic Boundary-Layer Transition with Ablation and Blowing,” *Journal of Spacecraft and Rockets*, Vol. 47, No. 2, 2012, pp. 225–237. <https://doi.org/10.2514/1.43926>.
- [10] Ifiti, H., Hermann, T., and McGilvray, M., “Transpiration Cooling At Mach 5 Employing Porous UHTC,” *Conference on Flight vehicles, Aerothermodynamics and Re-entry Missions and Engineering (FAR)*, 2019.
- [11] Dittert, C., Selzer, M., and Böhrk, H., “Flowfield and Pressure Decay Analysis of Porous Cones,” *AIAA Journal*, Vol. 55, No. 3, 2017, pp. 874–882. <https://doi.org/10.2514/1.J055298>.

- [12] Böhrk, H., and Beyermann, U., "Secure tightening of a CMC fastener for the heat shield of re-entry vehicles," *Composite Structures*, Vol. 92, No. 1, 2010, pp. 107–112. <https://doi.org/10.1016/j.compstruct.2009.07.002>.
- [13] Langener, T., Wolfersdorf, J. V., and Steelant, J., "Experimental Investigations on Transpiration Cooling for Scramjet Applications Using Different Coolants," *AIAA Journal*, Vol. 49, No. 7, 2011, pp. 1409–1419. <https://doi.org/10.2514/1.J050698>.
- [14] Schweikert, S., von Wolfersdorf, J., Selzer, M., and Hald, H., "Characterization of Actively Cooled Porous C/C Wall Segments According to Pressure Loss and Internal Temperature Distribution," *Proceedings of the 14th European Workshop on Thermal Protection Systems Hot Structures*, - April, ESAESTEC, Noordwijk, the Netherlands, 2013.
- [15] Löhle, S., Schweikert, S., and von Wolfersdorf, J., "Method for Heat Flux Determination of a Transpiration-Cooled Wall from Pressure Data," *Journal of Thermophysics and Heat Transfer*, Vol. 30, No. 3, 2016, pp. 567–572. <https://doi.org/10.2514/1.T4815>.
- [16] Bacos, M. P., "Carbon-carbon composites : oxidation behavior and coatings protection," *Le Journal de Physique IV*, Vol. 03, No. C7, 1993, pp. C7–1895–C7–1903. <https://doi.org/10.1051/jp4:19937303>.
- [17] Gascoin, N., "High temperature and pressure reactive flows through porous media," *International Journal of Multiphase Flow*, Vol. 37, No. 1, 2011, pp. 24–35. <https://doi.org/10.1016/j.ijmultiphaseflow.2010.09.001>.
- [18] Gascoin, N., Fau, G., Gillard, P., Kuhn, M., Bouchez, M., and Steelant, J., "Comparison of Two Permeation Test Benches and of Two Determination Methods for Darcy's and Forchheimer's Permeabilities," *Journal of Porous Media*, Vol. 15, No. 2012, 2012, pp. 705–720. <https://doi.org/10.1615/JPorMedia.v15.i8.10>.
- [19] Najmi, H., El-Tabach, E., Chetehouna, K., Gascoin, N., and Falempin, F., "Effect of flow configuration on Darcian and Forchheimer permeabilities determination in a porous composite tube," *International Journal of Hydrogen Energy*, Vol. 41, No. 1, 2016, pp. 316–323. <https://doi.org/10.1016/j.ijhydene.2015.10.054>.
- [20] Wang, J., and Vandeperre, L. J., "Deformation and Hardness of UHTCs as a Function of Temperature," *Ultra-High Temperature Ceramics: Materials for Extreme Environment Applications*, edited by W. G. Fahrenholtz, E. J. Wuchina, W. E. Lee, and Y. Zhou, John Wiley & Sons, Inc, Hoboken, NJ, 2014.
- [21] "BS EN ISO 4022:2006: Permeable sintered metal materials. Determination of fluid permeability," , 2006.
- [22] Lee, W. E., Giorgi, E., Harrison, R., Maître, A., and Rapaud, O., "Nuclear Applications for Ultra-High Temperature Ceramics and MAX Phases," *Ultra-High Temperature Ceramics*, John Wiley & Sons, Inc, Hoboken, NJ, 2014, pp. 391–415. <https://doi.org/10.1002/9781118700853.ch15>.
- [23] Nield, D. A., and Bejan, A., *Convection in Porous Media*, 4th ed., Springer, New York, NY, 2013. <https://doi.org/10.1007/978-1-4614-5541-7>.
- [24] Sutherland, W., "LII. The viscosity of gases and molecular force," *The London, Edinburgh, and Dublin Philosophical Magazine and Journal of Science*, Vol. 36, No. 223, 1853, pp. 507–531. <https://doi.org/10.1080/14786449308620508>.

- [25] Nelder, J. A., and Mead, R., "A Simplex Method for Function Minimization," *The Computer Journal*, Vol. 7, No. 4, 1965, pp. 308–313. <https://doi.org/10.1093/comjnl/7.4.308>.
- [26] "Filter-Elements: High porosity sintered parts SIKA-B," GKN Sinter Metals Filters GmbH, 2003.
- [27] Erdim, E., Akgiray, O., and Demir, I., "A revisit of pressure drop-flow rate correlations for packed beds of spheres," *Powder Technology*, Vol. 283, 2015, pp. 488–504. <https://doi.org/10.1016/j.powtec.2015.06.017>.
- [28] Ergun, S., "Fluid flow through packed columns," *Chemical Engineering Progress*, Vol. 48, 1952, pp. 89–94.
- [29] Sauter, J., *Die Grössenbestimmung der im Gemischnebel von Verbrennungskraftmaschinen vorhandenen Brennstoffteilchen*, VDI-Verlag, 1926.
- [30] Coleman, H. W., and Steele Jr., W. G., *Experimentation, Validation, and Uncertainty Analysis for Engineers*, John Wiley & Sons, Inc., Hoboken, NJ, USA, 2009. <https://doi.org/10.1002/9780470485682>.
- [31] Keyser, M. J., Conradie, M., Coertzen, M., and Van Dyk, J. C., "Effect of coal particle size distribution on packed bed pressure drop and gas flow distribution," *Fuel*, Vol. 85, No. 10-11, 2006, pp. 1439–1445. <https://doi.org/10.1016/j.fuel.2005.12.012>.
- [32] Koekemoer, A., and Luckos, A., "Effect of material type and particle size distribution on pressure drop in packed beds of large particles: Extending the Ergun equation," *Fuel*, Vol. 158, 2015, pp. 232–238. <https://doi.org/10.1016/j.fuel.2015.05.036>.
- [33] Macdonald, I. F., El-Sayed, M. S., Mow, K., and Dullien, F. A. L., "Flow through Porous Media-the Ergun Equation Revisited," *Industrial Engineering Chemistry Fundamentals*, Vol. 18, 1979, pp. 199–208. <https://doi.org/10.1021/i160071a001>.
- [34] Jørgensen, F. E., *How to Measure Turbulence with Hot-Wire Anemometers*, Aug. 2005.
- [35] Bruun, H. H., *Hot-Wire Anemometry : Principles and Signal Analysis*, Oxford University Press, 2002.
- [36] Aydin, M., and Leutheusser, H. J., "Very low velocity calibration and application of hot-wire probes," DISA Information, National Research Council of Canada, 1980.
- [37] Tsanis, I. K., "Calibration of hot-wire anemometers at very low velocities," Dantec Information, Feb. 1987.
- [38] Bhatia, J. C., Durst, F., and Jovanovic, J., "Corrections of hot-wire anemometer measurements near walls," *Journal of Fluid Mechanics*, Vol. 122, No. -1, 2006, pp. 411–431. <https://doi.org/10.1017/S0022112082002286>.
- [39] Moffat, R. J., "Describing the uncertainties in experimental results," *Experimental Thermal and Fluid Science*, Vol. 1, No. 1, 1988, pp. 3–17. [https://doi.org/10.1016/0894-1777\(88\)90043-X](https://doi.org/10.1016/0894-1777(88)90043-X).